

Inertial focusing of spherical particles: The effects of rotational motion

Dmitry Alexeev¹, Sergey Litvinov², Athena Economides³, Lucas Amoudruz², Mehmet Toner^{4,*}, and Petros Koumoutsakos^{1,†}

¹NVIDIA, Zurich, Switzerland

²Computational Science and Engineering Laboratory, *Harvard University*, Cambridge, Massachusetts 02138, USA

³Institute of Neuropathology, University Hospital Zurich, *University of Zurich*, Zurich, Switzerland

⁴Center for Engineering in Medicine and Surgical Services, *Massachusetts General Hospital*, Harvard Medical School, Boston, Massachusetts 02114, USA



(Received 19 August 2024; accepted 7 March 2025; published 14 May 2025)

The identification of cells and particles based on their transport properties in microfluidic devices is crucial for numerous applications in biology and medicine. Neutrally buoyant particles transported in microfluidic channels migrate laterally toward stable locations due to inertial effects. However, the effect of the particle and flow properties on these focusing positions remain largely unknown. We conduct large scale simulations with dissipative particle dynamics, demonstrating that freely moving particles exhibit significant differences in their focusing patterns from particles that are prevented from rotation. In circular pipes, we observe drastic changes in rotating versus nonrotating focusing positions. We demonstrate that rotation-induced lateral lift force is significant, unlike previously believed, and is linearly dependent on the rotation magnitude. A simple phenomenological explanation extending existing theories is presented, that agrees well with our numerical findings. In square ducts, we report four face-centered stable positions for rotating particles, in accordance with experimental studies on a range of Reynolds numbers $50 \leq Re \leq 200$. However, nonrotating particles stay scattered on a concentric one-dimensional annulus, revealing qualitatively different behavior with respect to the free ones. Our findings suggest new designs for microparticle and cell sorting in inertia-based microfluidics devices.

DOI: [10.1103/PhysRevFluids.10.054202](https://doi.org/10.1103/PhysRevFluids.10.054202)

I. INTRODUCTION

Inertial microfluidics is opening up numerous possibilities for fast and clogging-free focusing and sorting of biological cells and microparticles [1–4]. In inertial transport, particles migrate across streamlines and stabilize in certain lateral locations in the flow field. Inertia is essential in this cross-streamline movement, as lateral translation is hindered in Stokes flow [5,6].

In contrast to traditional cell sorting techniques [6], such as filtering [7] or exploitation of lateral displacement [8], inertial manipulation is free from externally applied fields or direct mechanical interaction with obstacles. The first studies on inertial migration were reported in the work of Segré and Silberberg [9]. These studies reported that small particles submerged in the circular pipe flow concentrate at the annulus of radius $\sim 0.6R$. More recently, other studies [10–13] have shown that these migrations occur in channels of any cross-section shape and at a wide range of Reynolds numbers (from 10 to 1000), for rigid particles, liquid droplets, and cells.

*Also at Shriners Hospitals for Children, Boston, MA 02114, USA.

†Contact author: petros@seas.harvard.edu

Interestingly, the lateral positions where the particles focus vary significantly with Reynolds numbers, channel geometry and particle size. Matas *et al.* [14,15] showed experimentally that the equilibrium particle position in circular pipe shifts outward as the channel Reynolds number increases. Choi *et al.* [16] confirmed that bigger particles stabilize closer to the center of the pipe. The same behavior was reported for square channels [11], with, however, an important difference: only four stable lateral positions are observed at intermediate Reynolds numbers [17], in contrast to the stable annulus in circular pipes. Migration to those points happens in two stages: during the first, faster, stage the particles gather into a deformed ring, similar to the original Segré-Silberberg annulus. During the second, slower, stage the particles move toward the four points next to the centers of the channel faces. This focusing pattern makes it possible to use the square channels to precisely collect microscale particles and cells at the channel outlet and allows for fast and noninvasive methods for sorting and filtering [11].

As the small inertial effects are difficult to study analytically, various restrictions and assumptions on the problem setup were made in the theoretical works. In particular, the particle size was assumed to be much smaller than the diameter of the channel [18,19]. However, the experimental verification of these findings is complicated, as small particles show very slow lateral migration. Recent works [20,21] present an asymptotic theory for larger particles in square channels. Their analysis captures experimental trends, however, [22] displays notable inaccuracies in the near-wall region and is still limited to relatively small particles: ~ 0.15 of the channel size. Overall, there is a consensus among the theoretical works that the influence of particle rotation on the lift force, and thus on the focusing position, is negligible. Numerical studies alleviate the restriction on the particle size, shape, and channel cross section [23]. Feng [24] used two-dimensional finite element simulations to assess the forces acting on a rigid particle in Couette and Poiseuille flows, confirming that there exists a certain stable lateral position. They identified three main components of the lift force: wall force, force due to the nonuniform shear rate, and force associated with the particle rotation (Magnus effect), noting once again that the rotation-attributed force is much smaller than the rest. Chun and Ladd [25] performed a three-dimensional study of the particle focusing positions in the square duct. Although they observed the two-stage migration process, their final stable points were both corners and face centers even for low Reynolds around 100, which contradicts experiments. A good agreement to the experimental data [17] was achieved by Nakagawa [22] with the immersed boundary method. They demonstrated that up to the critical channel Reynolds number of about 260, only the face centers are stable, and after that corners become stable too. Liu [26] carried out experimental and numerical study of the particle behavior in the channel with rectangular cross section and observed similar focusing patterns as for the square channel. They also presented results for different particle sizes, confirming that bigger particles tend to stay closer to the channel center. Harding and Stokes [27] studied the inertial focusing of neutrally buoyant spherical particles in curved microfluidic ducts at moderate Dean numbers, using regular perturbation expansions. They found that variations in the Dean number cause a change in the axial velocity profile of the background flow which influences the inertial lift force on a particle. More recently, the authors also studied the effects of trapezoidal ducts [28]. In [29] simulations of particulate flows in square ducts with oblate and prolate particles revealed that inertial migration causes particles to focus in specific cross-sectional regions, with nonspherical particles occupying different positions than spherical ones. Investigations in a wavy channel [30] demonstrated that interactions between the zeroth-order lift force and the particle-free flow largely determine the focusing locations.

In the present work we employ the method of dissipative particle dynamics (DPD) [31–34] to study the inertial focusing of rigid particles in the circular and square channel flows. Our results agree well with experimental data and previous numerical studies. In contrast to the recent study by Huang *et al.* [35], we observe a broad range of Re and particle sizes where DPD is applicable (see the Supplemental Material [36], which also contains Refs. [37–42]).

We investigate the influence of particle rotation on migration patterns within a circular pipe. Our study examines a range of particle sizes and channel Reynolds numbers. Contrary to the commonly held assumption that rotation-induced forces are negligible, we observe significant differences in

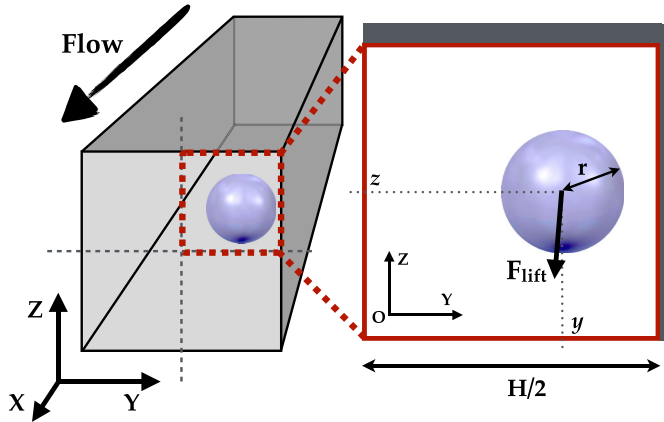


FIG. 1. The particle is translated with the flow along Ox and experiences lateral forces along Oy and Oz . Its position is characterized by y and z with origin at the pipe center.

the migration behavior of freely rotating and nonrotating particles, consistent with experimental findings [43]. Our results reveal that the rotation-induced force consistently acts toward the pipe wall, aligning with the force generated by the nonuniform shear rate. Starting with the latter force explanation by Feng [24], we take into account flow distortion by the particle to arrive at a similar explanation for the order of magnitude and direction of the rotation-induced force. We also provide a scaling law which describes the force due to rotation in terms of the channel Reynolds number, particle size, and angular velocity. Linear dependence of this force on the rotation agrees with our explanation.

In the square duct we demonstrate that the midface equilibrium positions of the particles are reached in the previously reported two-stage process. We find that the particles with inhibited rotation show no secondary migration stage, staying scattered at the concentric annulus. We also show that unlike hypothesised by Zhou [44], the secondary migration is not solely governed by the particle rotation, but rather by more complex interplay of the rotation and wall force. Our findings unveil possibilities for novel designs of microfluidic filtering devices, allowing separation of objects based on the size and rotation.

II. METHODS

We consider straight pipes of circular and square cross sections filled with a Newtonian, incompressible fluid, with periodic boundary conditions to mimic long pipes. We model the suspended particle as a spherical, nondeformable object with the same density as the fluid. To simulate this system, we employ the DPD method within the software Mirheo [45], which has been extensively validated for incompressible flows with suspended biological cells [46,47], and suspended rigid objects [45,48]. In addition, several cases of particles in circular pipes and square ducts are validated against experimental work [16,17] and numerical work [11,22,26] in the Supplemental Material [36]. The parameters of the numerical model that were used in this work are reported in the Supplemental Material [36]. The simulation describes the neutrally buoyant spherical particles of radius r moving in the channel flow with translational velocity \mathbf{V} and rotational velocity $\boldsymbol{\Omega}$ (Fig. 1). We define $\mathbf{F}_{\text{particle}} = \mathbf{F}_f + \mathbf{F}_{\text{ext}}$ as the total force acting on the particle, including the hydrodynamic force and externally applied force; $\mathbf{T}_{\text{particle}} = \mathbf{T}_f + \mathbf{T}_{\text{ext}}$ —the total torque acting on the particle, including the hydrodynamic torque and externally applied torque. Moreover, \mathbf{u} denotes the fluid velocity, p —pressure, ρ —density, and $\nu = \eta/\rho$ —kinematic viscosity. Finally, we assume no-slip boundary conditions on the channel walls and the particles.

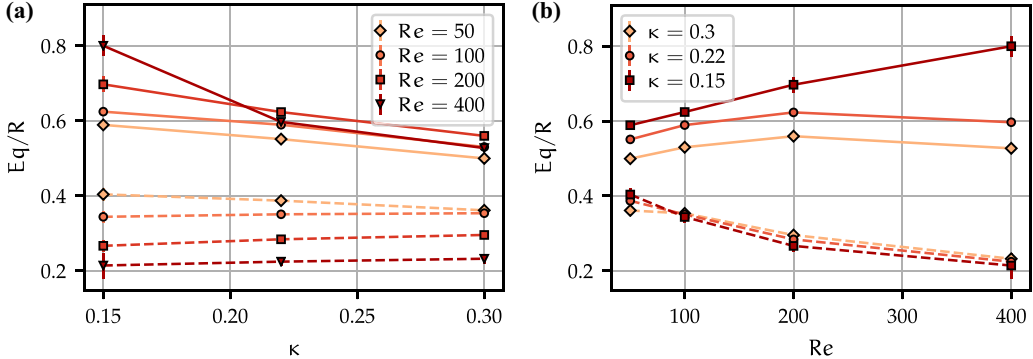


FIG. 2. Equilibrium positions Eq of freely rotating (solid lines) and nonrotating (dashed lines) particles against particle-to-channel size ratio κ (a) and against channel Reynolds number Re (b) in a circular pipe.

We denote the square channel side length as H and for uniformity the circular pipe radius as $R = H/2$. We also introduce the particle-to-channel size ratio as $\kappa = 2r/H = r/R$. The flow is driven along the channel axis by the pressure gradient ∇p_{ext} . We define the channel Reynolds number as $Re = U_{\text{avg}}\rho H/\eta$, where U_{avg} is the average velocity of the undisturbed flow,

$$U_{\text{avg}}^{\text{circle}} = \frac{H^2 \nabla p_{\text{ext}}}{32\eta}, \quad U_{\text{avg}}^{\text{square}} = \frac{H^2 \nabla p_{\text{ext}}}{28.45415\eta}. \quad (1)$$

The nondimensional lift coefficient for a sphere experiencing lateral force F_l is given by

$$C_l = \frac{F_l H^2}{\rho U_{\text{avg}}^2 (2r)^4}. \quad (2)$$

Furthermore we define the particle Reynolds number as $Re_p = \kappa^2 Re$ [24]. To compute the forces acting on the particle at a given lateral position, we restrict the particle motion along Oy and Oz axes, while allowing it to freely translate with the flow along Ox . The instantaneous forces acting on the particle along Oy and Oz are noisy due to the stochastic nature of the DPD method. Therefore, we average these forces over time after the simulation has equilibrated. The simulation is considered at equilibrium after the velocity of the particle along x reaches a constant value. We use periodic boundary condition in x and keep the length of the channel at least 15 times larger than the particle diameter [22].

We interpolate the averaged forces with gaussian process regression (GPR) [49]. This technique allows us to take the uncertainty in the mean estimator and provide error estimates in the interpolation.

III. RESULTS AND DISCUSSION

A. Circular pipe

We first study the inertial migration of particles in the circular pipe. We compute the lateral lift forces for multiple parameter combinations of $Re \in \{50, 100, 200, 400\}$ and $\kappa \in \{0.15, 0.22, 0.3\}$. The particle is allowed to rotate in general, unless otherwise specified.

In accordance with the previous numerical and experimental studies [11,26], we observe that the bigger particles equilibrate closer to the channel axis [Fig. 2(a)], and that the focusing position shifts outwards when Re is increased [Fig. 2(b)], with the exception of higher Re at large κ . When the Reynolds number increases beyond 200, large particles with $\kappa \in \{0.22, 0.3\}$ equilibrate closer to the channel axis, than at $Re = 200$. Oliver *et al.* [43] report a similar behavior with $\kappa = 0.24$ and $\kappa = 0.32$ (see also Fig. 3).

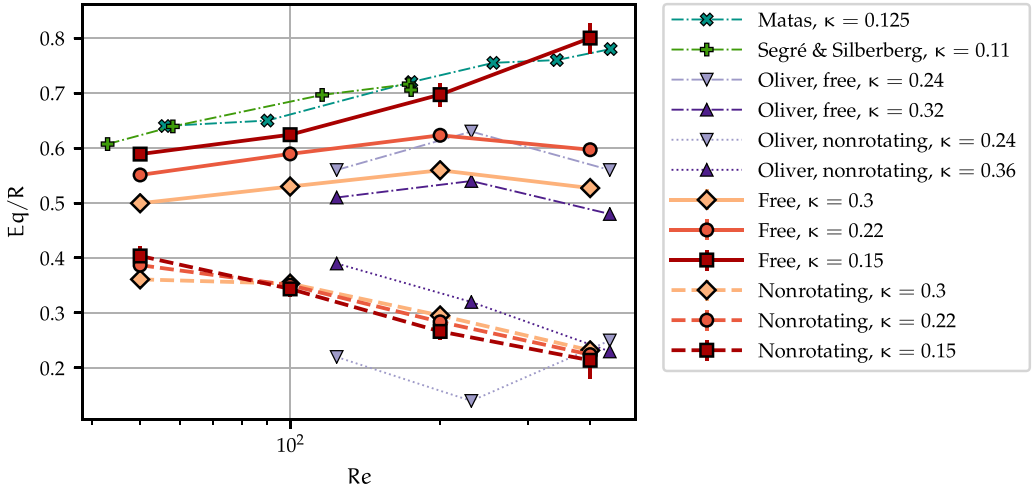


FIG. 3. Experimental data for different κ and Re , compared to our results. Matas data is from [14], Segré and Silberberg data is from [9], Oliver data is from [43]. Data from Oliver corresponds to only two particles per experiment. Solid lines represent our results for freely rotating particles, dashed lines—our nonrotating ones. Dash dotted are experimental rotating, dotted are experimental nonrotating.

In the absence of particle rotation, the equilibrium position of the particle is closer to the channel axis than in the rotating case (see Fig. 2). This result agrees with previous numerical findings [24,50]. However, we find a much more pronounced change compared to the rotating case than previously reported. We conclude from this result that the force due to rotation of the particle is larger than reported before [11,13]. As also depicted in the Supplemental Material [36], the lift forces for the rotation-free particles are negatively shifted for almost all the cases and all the different particle positions y/R . That results in the fact that, for example, the small particle ($\kappa = 0.15$) at $Re = 200$ ($Re_p = 4.5$) changes its equilibrium position from the default $0.7R$ to $0.28R$.

The only experimental study found by the authors with nonrotating particles [43] agrees well with our results. Particles during that experiment were prevented from rotation using magnetic field. Observed difference in the focusing positions can hardly be quantified due to the very small size of the dataset, but the major trends are indisputable. Figure 3 compares available experimental data at κ similar to ours with our results.

To explain the rotation significance, we have to recall the current understanding of the migration mechanism. According to numerous works [2,6,24], the lateral force acting on a particle can be separated into two components: the wall force F_l^{wall} , which always pushes the particle away from the wall, and the force due to the nonuniform flow shear rate F_l^{shear} . While the wall repulsion is observed and studied in various problems with sphere translating parallel to the wall [51–53], the shear-induced lift is not understood well. Its classical explanation attributed to Feng [24] is sketched in Fig. 4(a). Looking at the undisturbed flow profile relative to the moving particles, one can notice the higher and lower speed regions (shown respectively on the bottom and top of the sketch). We consider two streamlines that are on each side of the particle but close to each other upstream, where they share the same velocity and pressure. Thus, applying the Bernoulli principle along each streamline, the difference in velocity on each side of the particle yields a larger pressure above the particle than below it [24]. This results in a net force directed toward the wall.

However, the finite-sized particle always disturbs the flow around itself. The nonrotating particle slows down the relative flow both above and below [Fig. 4(b)], while the rotating one [Fig. 4(c)] perturbs the background flow less significantly. Note that the actual data from our simulation in Fig. 4(d) corresponds well with this statement. This leads to the fact that in the case of rotation the

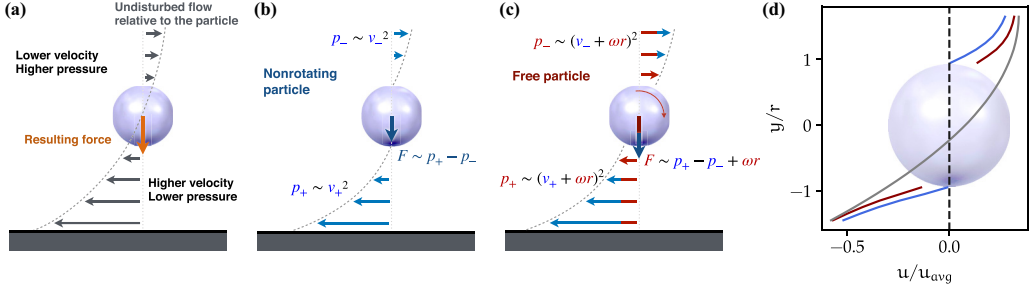


FIG. 4. The lift due to the non-uniform flow shear. (a) Common explanations only takes into account the undisturbed flow. However, disturbed flow over the nonrotating particle [(b), in blue] or freely rotating one [(c), blue and red] is different, being faster close to the surface for the case of the free rotation. This leads to extra lift force attributed to the spinning (in red). (d) Numerical experiment shows a similar flow velocity profile relative to the particle. Simulation parameters: $Re = 100$, $\kappa = 0.22$, $y/R = 0.4$ ($Re_p = 4.84$). The curves represent averaged streamwise flow velocity along a line through the sphere center parallel to Oy , blue is nonrotating particle case, red is freely rotating one, and black is undisturbed flow profile far away from the particle.

velocity magnitudes both below and above the particle are higher, which, assuming Bernoulli-like quadratic pressure dependence on velocity, results in higher pressure difference across the sphere. Simple calculations lead to $F_l^{\text{shear}}(\omega) \sim \Delta p \sim \Delta p_0 + C\omega$, where p_0 is the pressure difference in the case of absence of rotation, ω is the sphere angular velocity, and C is a constant.

This hypothesis predicts rotation to strengthen the lift toward the wall, as we observe. It also implies linear dependence between the rotation-induced lift force $F_l^{\text{rot}}(\omega) = F_l(\omega) - F_l(0)$ and the angular velocity ω . This behavior is indeed observed, as depicted in Fig. 5. The plot shows scaled difference in the lift coefficient $C_l^{\text{rot}}(\omega) = C_l(\omega) - C_l(0)$ against the rate of rotation $\omega/\omega_{\text{ref}}$. Here $\omega_{\text{ref}} = \dot{\gamma}/2$ is the reference angular velocity (observed when for a sphere rotating in the simple Stokes shear flow) and $\dot{\gamma}$ is the shear rate at the sphere center. We observe an excellent collapse of all the force-rotation lines for different Re and κ when $y < R/2$, suggesting a universal scaling law for the rotation-induced force contribution far from the wall.

In that case, we give the following empirical expression for the rotation-induced lift coefficient:

$$C_l^{\text{rot}}(\omega) = K \frac{\omega}{\omega_{\text{ref}}} (1 - \kappa)^{1/2} Re^{1/3} (y/R), \quad (3)$$

where linear least square fit for $y < R/2$ leads to $K \approx 5.74$. Moreover, it suggests that the rotation-induced part of the lift has the same order of magnitude as the pure $F_l^{\text{shear}}(0)$, since in the case of the freely rotating particles, its angular velocity is reasonably close to the reference ω_{ref} . More detailed force profiles available in the Supplemental Material [36] support that idea.

Finally, the focusing positions of the nonrotating particles show different behavior with respect to Re and κ . From Fig. 2(a) we see that bigger nonrotating particles no longer move closer to the pipe axis. Instead, the focusing position stays roughly constant, only changing noticeably for the highest $Re = 400$. More interestingly, increasing Re moves the focusing positions further away from the wall, which is the opposite of the freely rotating particles [see Fig. 2(b)]. The exact reasons of such behavior remain an open question and require further studies.

B. Square duct

For the case of the square cross section we only vary $Re \in \{50, 100, 200\}$, while keeping $\kappa = 0.22$ to reduce the computational time. This corresponds to particle Reynolds numbers $Re_p \in \{2.42, 4.84, 9.68\}$. For the sake of brevity we hereafter focus on $Re = 100$, noting that the general findings for the other Reynolds numbers are similar according to our results. Figure 6(a) shows the map of lift forces acting on a freely rotating particle at different lateral positions. Due to the

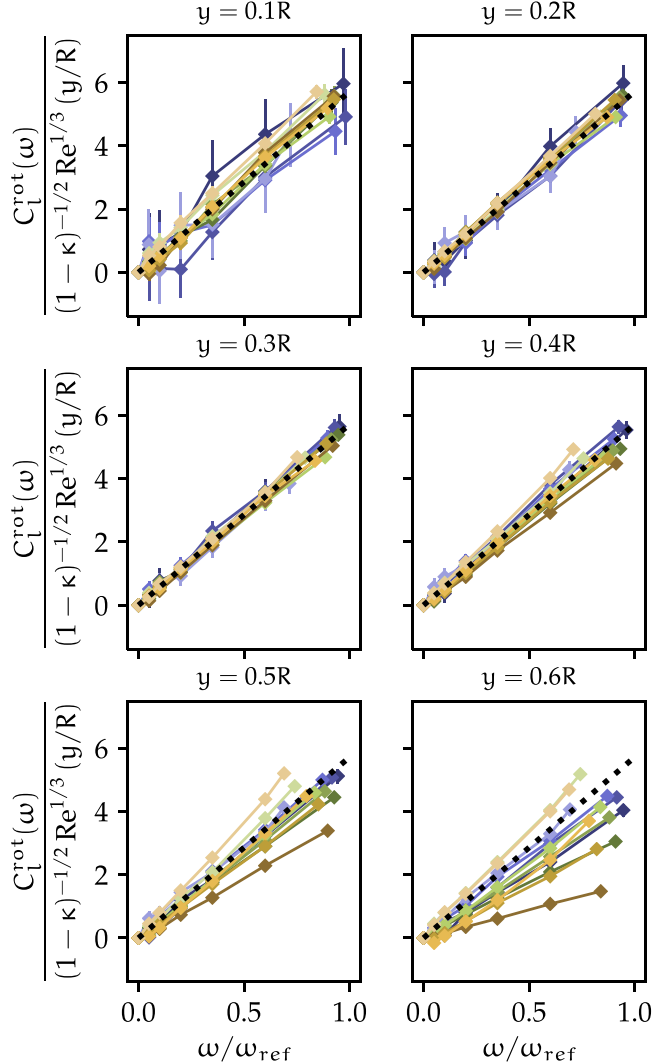


FIG. 5. Scaled rotation-induced lift coefficient for all the studied Re and κ is proportional to the rotation velocity ω . Linear dependence remains even when particles are close to the wall, $y > 0$, however, the slope changes in that case. Dashed line is the empirical fit for $y < 0.4R$.

symmetry of the square channel, we only perform simulations for one half of the cross-section quadrant ($y > 0, z > 0, z \leq y$). For illustrative purposes, we plot forces for the full quadrant by mirroring them along the diagonal $y = z$.

Analysis of the lateral force vector field reveals two different types of equilibrium positions consistent with the previous experimental and numerical studies [17,22,26,54]: the corner position is an unstable saddle point, as some force vectors point out of it, and the midedge position is stable. The streamline starting in the unstable equilibrium and finishing in the stable one (separatrix) divides the lateral positions into two zones: if the particle starts close to the pipe axis, it will initially migrate toward the wall, while the particle starting between the separatrix and the wall will move to the center. While on the separating streamline, the particle will continue moving along it until it reaches the stable edge equilibrium. As a characteristic of the secondary migration speed, in Fig. 6(c) we

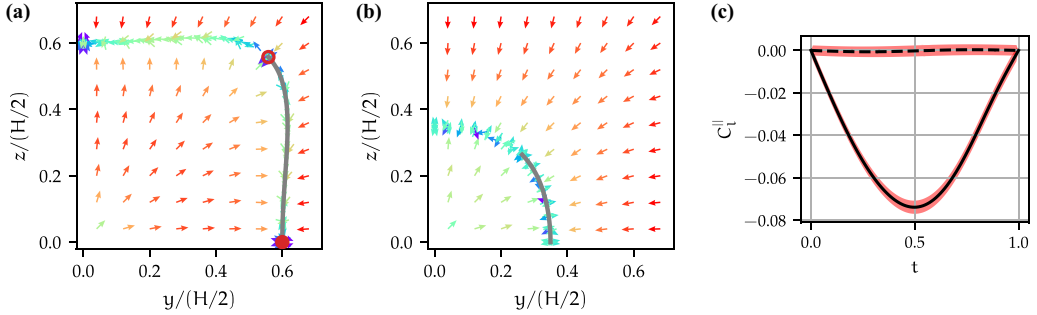


FIG. 6. (a), (b) Map of the lateral forces acting on a sphere, respectively rotating and nonrotating, in a square channel at $Re = 100$, $\kappa = 0.22$. Each arrow corresponds to one simulation and shows the direction of the force, while color marks the magnitude (red is higher). Open circle is the unstable equilibrium position, full—stable, gray line is the streamline connecting them (separatrix). (c) Lift force along the separatrix. Ox axis is in parametric units such that the separatrix manifold is $S = \{(x(t), y(t))\}$ with $t = 0$ the edge equilibrium, $t = 1$ the corner one.

plot the force acting on the particle along the separatrix curve. The parametrization of the separatrix $S(t) = (x(t), y(t))$ is such that $S(0)$ is the stable edge-center equilibrium, and $S(1)$ is the unstable one. The force along the separatrix can therefore be calculated as follows:

$$F_l^{\parallel}(t) = F_l(S(t)) \cdot \left(\frac{dS}{dt}(t) \left| \frac{dS}{dt}(t) \right|^{-1} \right). \quad (4)$$

Here, \cdot means the dot product.

We do not compare fast and slow migration as it has been done previously [22], but instead we draw our attention to the effect of inhibited rotation. Figure 6(b) shows the lateral force map for the nonrotating particle. In this case we can not anymore clearly identify specific equilibrium points:

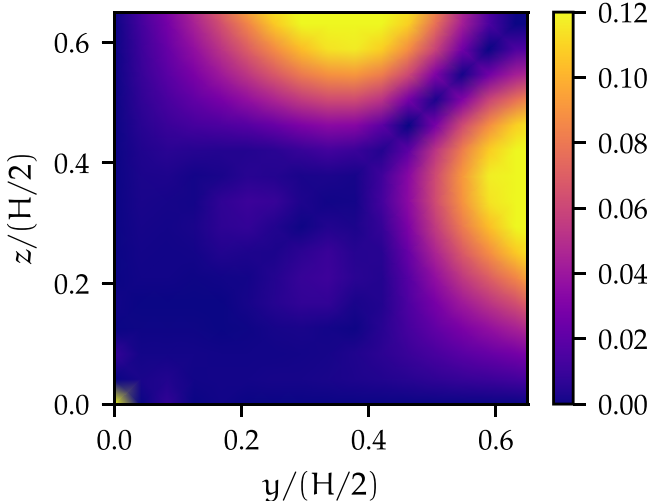


FIG. 7. Heat map corresponds to the dot product of unit vectors in the direction of the rotation-induced force F_l^{rot} and angular velocity ω , representing their alignment.

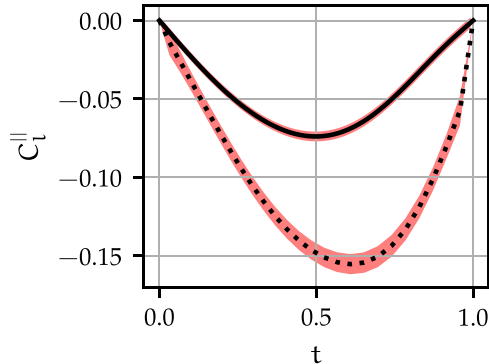


FIG. 8. Force along the separatrix driving a particle from the corner to the edge equilibrium (solid line) increases if the particle is prevented from rotating normally to the separatrix curve (dashed).

instead we observe a one-dimensional equilibrium manifold. All the points on that line result in zero force and migration velocity, as seen in Fig. 6(c). Hence, we conclude that the particles prevented from rotation undergo no secondary migration.

One can consequently think that rotation is responsible for the particle movement along the separatrix toward the stable equilibrium (see, e.g., [44]). To assess this hypothesis, we take two steps. As the first step, we show that the direction of the rotation-induced force is highly correlated with the vector, normal to the particle's angular velocity. We subtract two force fields (with and without rotation) and compute the angle ϕ between the difference \mathbf{F}^{diff} and the angular velocity vector of the freely rotating particle. Figure 7 shows that the angle between the two vectors is perpendicular within less than 10° , with more pronounced discrepancy closer to the wall. This observation suggests that small changes in rotation induce force roughly orthogonal to that change, and that only the rotation orthogonal to the separatrix line can cause the secondary migration.

In the second step, we check our supposition by carrying out simulations with modified rotation of the particles on the separatrix. In these simulations, we allow the particles to freely rotate tangentially to the separatrix line, while the normal component of the rotation is modified and set to zero. In agreement with our previous conclusion, the resulting force only differs tangentially to the separatrix, while the normal component (that would have changed the location of the separatrix) stays zero. However, contrary to our initial hypothesis, the force of the secondary migration is increased, see Fig. 8. Indeed, such direction of the rotation-induced force agrees with previous works [24,43], and with our results for the circular pipe. This result means that the secondary migration is not solely attributed to the rotation, but is instead governed by the interplay of all the forces including wall force, and shear- and rotation-induced components. The exact physical picture could be the focus of later studies.

Finally, the fact that rotation produces close to orthogonal force allows us to consider modification of the equilibrium positions by manipulating rotation. A similar approach was presented in [50], however, only in 2D. We apply external torque \mathbf{T}^{ext} in the positive direction of the Oy axis which results in shifting the lateral force field and breaking the symmetry (see Fig. 9). The extra rotation overcomes the intrinsic force of the secondary migration and results in elimination of the stable equilibria at $y = 0$. The corner positions disappear as well, and the top one of the remaining two equilibria becomes unstable. Therefore, all the particles experiencing external torque (high enough to overcome the natural inertial forces) will now gather at the unique lateral position.

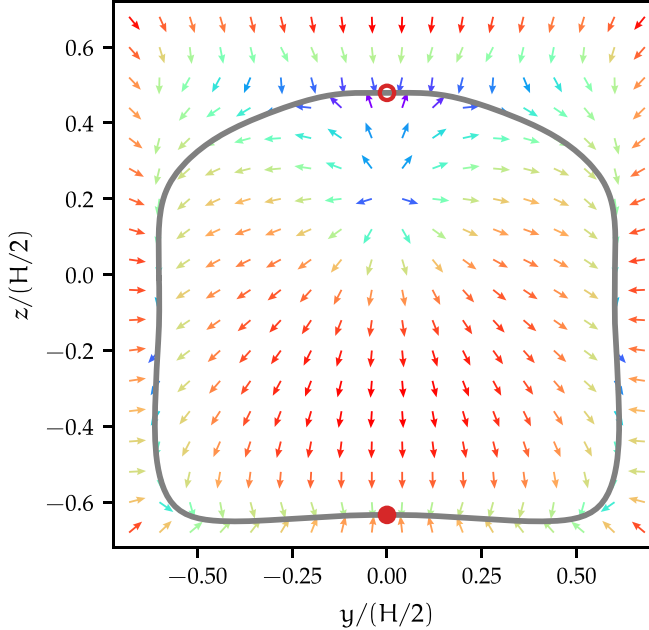


FIG. 9. When extra torque is applied to a particle, the equilibrium positions change, with only a single stable edge equilibrium position apparent. Arrows are a map of the lateral forces acting on a sphere in a square channel at $\text{Re} = 100$, $\kappa = 0.22$ ($\text{Re}_p = 4.84$) with applied external torque along Oy : $T_y^{\text{ext}} = 0.75\rho U_{\text{avg}}^2(2r)^5 H^{-2}$. Each arrow corresponds to one simulation and shows the direction of the force, while color marks the magnitude (red is higher). The gray line is the equilibrium manifold.

IV. CONCLUSIONS

In this work we employed the DPD method to numerically examine lateral inertial migration of rigid spherical particles and focused our attention to the role of particle rotation in the migration. Our results for circular pipe show that rotation significantly changes particle equilibrium position despite the common thinking that its contribution is negligible. Moreover, we observed that nonrotating particles focus closer to the pipe axis with increased Reynolds, which is the opposite to the freely rotating ones. We also proposed phenomenological scaling of the rotation-induced lift coefficient with Re and κ .

Additionally, we studied channels with a square cross section. We found that particles with restricted rotation undergo no secondary migration, remaining on the equilibrium annulus. Moreover, we proved wrong a seemingly logical hypothesis that rotation solely moves particles during the second migration stage: instead this stage seems to be governed by the interplay of all the forces in the system, with rotation actually slowing the migration along the annulus. Finally, we proposed a simple way to modify the focusing in the square duct, removing all but just one equilibrium position. Our findings suggest inertial microfluidic designs that exploit the rotation of the focusing particles.

ACKNOWLEDGMENT

We acknowledge the computational resources provided by the Swiss National Supercomputing Center (CSCS) under Project IDs ch7, and by the FASRC Cannon cluster, supported by the FAS Division of Science Research Computing Group at Harvard University.

- [1] D. Di Carlo, Inertial microfluidics, *Lab Chip* **9**, 3038 (2009).
- [2] J. Zhang, S. Yan, D. Yuan, G. Alici, N. T. Nguyen, M. Ebrahimi Warkiani, and W. Li, Fundamentals and applications of inertial microfluidics: A review, *Lab Chip* **16**, 10 (2016).
- [3] S. F. Berlanda, M. Breitfeld, C. L. Dietsche, and P. S. Dittrich, Recent advances in microfluidic technology for bioanalysis and diagnostics, *Anal. Chem.* **93**, 311 (2021).
- [4] T. Peng, J. Qiang, and S. Yuan, Sheathless inertial particle focusing methods within microfluidic devices: A review, *Front. Bioeng. Biotechnol.* **11**, 1331968 (2024).
- [5] H. A. Stone, A. D. Stroock, and A. Ajdari, Engineering flows in small devices: microfluidics toward a lab-on-a-chip, *Annu. Rev. Fluid Mech.* **36**, 381 (2004).
- [6] J. M. Martel and M. Toner, Inertial focusing in microfluidics, *Annu. Rev. Biomed. Eng.* **16**, 371 (2014).
- [7] S. M. McFaul, B. K. Lin, and H. Ma, Cell separation based on size and deformability using microfluidic funnel ratchets, *Lab Chip* **12**, 2369 (2012).
- [8] N. M. Karabacak, P. S. Spuhler, F. Fachin, E. J. Lim, V. Pai, E. Ozkumur, J. M. Martel, N. Kojic, K. Smith, P.-i. Chen, J. Yang, H. Hwang, B. Morgan, J. Trautwein, T. A. Barber, S. L. Stott, S. Maheswaran, R. Kapur, D. Haber, and M. Toner, Microfluidic, marker-free isolation of circulating tumor cells from blood samples, *Nat. Protoc.* **9**, 694 (2014).
- [9] G. Segre and A. Silberberg, Behaviour of macroscopic rigid spheres in Poiseuille flow part 2. Experimental results and interpretation, *J. Fluid Mech.* **14**, 136 (1962).
- [10] A. A. S. Bhagat, S. S. Kuntaegowdanahalli, and I. Papautsky, Continuous particle separation in spiral microchannels using dean flows and differential migration, *Lab Chip* **8**, 1906 (2008).
- [11] D. Di Carlo, J. F. Edd, K. J. Humphry, H. A. Stone, and M. Toner, Particle segregation and dynamics in confined flows, *Phys. Rev. Lett.* **102**, 094503 (2009).
- [12] S. C. Hur, N. K. Henderson-Maclennan, E. R. B. McCabe, and D. Di Carlo, Deformability-based cell classification and enrichment using inertial microfluidics, *Lab Chip* **11**, 912 (2011).
- [13] H. Amini, W. Lee, and D. Di Carlo, Inertial microfluidic physics, *Lab Chip* **14**, 2739 (2014).
- [14] J. P. Matas, J. F. Morris, E. Guazzelli, and É. Guazzelli, Inertial migration of rigid spherical particles in Poiseuille flow, *J. Fluid Mech.* **515**, 171 (1999).
- [15] J. Matas, J. Morris, and E. Guazzelli, Lateral forces on a sphere, *Oil Gas Sci. Technol.* **59**, 59 (2004).
- [16] Y. S. Choi and S. J. Lee, Holographic analysis of three-dimensional inertial migration of spherical particles in micro-scale pipe flow, *Microfluid Nanofluid* **9**, 819 (2010).
- [17] K. Miura, T. Itano, and M. Sugihara-Seki, Inertial migration of neutrally buoyant spheres in a pressure-driven flow through square channels, *J. Fluid Mech.* **749**, 320 (2014).
- [18] P. Saffman, The lift force on a small sphere in a slow shear flow, *J. Fluid Mech.* **22**, 385 (1965).
- [19] E. S. Asmolov, The inertial lift on a spherical particle in a plane Poiseuille flow at large channel Reynolds number, *J. Fluid Mech.* **381**, 63 (1999).
- [20] K. Hood, S. Lee, and M. Roper, Inertial migration of a rigid sphere in three-dimensional Poiseuille flow, *J. Fluid Mech.* **765**, 452 (2015).
- [21] K. Hood, S. Kahkeshani, D. Di Carlo, and M. Roper, Direct measurement of particle inertial migration in rectangular microchannels, *Lab Chip* **16**, 2840 (2016).
- [22] N. Nakagawa, T. Yabu, R. Otomo, A. Kase, M. Makino, T. Itano, and M. Sugihara-Seki, Inertial migration of a spherical particle in laminar square channel flows from low to high Reynolds numbers, *J. Fluid Mech.* **779**, 776 (2015).
- [23] R. Shi, Numerical simulation of inertial microfluidics: A review, *Eng. Appl. Comput. Fluid Mech.* **17**, 2177350 (2023).
- [24] J. Feng, D. D. Joseph, H. H. Hu, and D. D. Joseph, Direct simulation of initial value problems for the motion of solid bodies in a Newtonian fluid. Part 2. Couette and Poiseuille flows, *J. Fluid Mech.* **277**, 271 (1994).
- [25] B. Chun and A. J. C. Ladd, Inertial migration of neutrally buoyant particles in a square duct: An investigation of multiple equilibrium positions, *Phys. Fluids* **18**, 031704 (2006).
- [26] C. Liu, G. Hu, X. Jiang, and J. Sun, Inertial focusing of spherical particles in rectangular microchannels over a wide range of Reynolds numbers, *Lab Chip* **15**, 1168 (2015).

- [27] B. Harding and Y. M. Stokes, Inertial focusing of spherical particles in curved microfluidic ducts at moderate dean numbers, *J. Fluid Mech.* **957**, A17 (2023).
- [28] B. Harding, Y. M. Stokes, and R. N. Valani, Inertial focusing dynamics of spherical particles in curved microfluidic ducts with a trapezoidal cross section, *SIAM J. Appl. Dyn. Syst.* **23**, 1805 (2024).
- [29] T. Hafemann and J. Fröhlich, Inertial migration of non-spherical particles in straight microfluidic channels, *Phys. Fluids* **35**, 013328 (2023).
- [30] X. Mao, I. Bischofberger, and A. Hosoi, Particle focusing in a wavy channel, *J. Fluid Mech.* **968**, A25 (2023).
- [31] P. J. Hoogerbrugge and J. M. V. A. Koelman, Simulating microscopic hydrodynamic phenomena with dissipative particle dynamics, *Europhys. Lett.* **19**, 155 (1992).
- [32] I. V. Pivkin, B. Caswell, and G. E. Karniadakis, Dissipative particle dynamics, *Rev. Comput. Chem.* **27**, 85 (2010).
- [33] P. Español and P. B. Warren, Perspective: Dissipative particle dynamics, *J. Chem. Phys.* **146**, 150901 (2017).
- [34] B. Owen and T. Krüger, Numerical investigation of the formation and stability of homogeneous pairs of soft particles in inertial microfluidics, *J. Fluid Mech.* **937**, A4 (2022).
- [35] Y. Huang, R. L. Marson, and R. G. Larson, Inertial migration of a rigid sphere in plane Poiseuille flow as a test of dissipative particle dynamics simulations, *J. Chem. Phys.* **149**, 164912 (2018).
- [36] See Supplemental Material at <http://link.aps.org/supplemental/10.1103/PhysRevFluids.10.054202> for a detailed description and verification of the numerical method, simulation parameters, additional figures, and convergence analysis.
- [37] P. Español, Hydrodynamics from dissipative particle dynamics, *Phys. Rev. E* **52**, 1734 (1995).
- [38] R. D. Groot and P. B. Warren, Dissipative particle dynamics: Bridging the gap between atomistic and mesoscopic simulation, *J. Chem. Phys.* **107**, 4423 (1997).
- [39] X. Fan, N. Phan-Thien, S. Chen, X. Wu, and T. Y. Ng, Simulating flow of DNA suspension using dissipative particle dynamics, *Phys. Fluids* **18**, 063102 (2006).
- [40] D. Rozmanov and P. G. Kusalik, Robust rotational-velocity-verlet integration methods, *Phys. Rev. E* **81**, 056706 (2010).
- [41] M. Revenga, I. Zúñiga, P. Español, and I. Pagonabarraga, Boundary models in DPD, *Int. J. Mod. Phys. C* **09**, 1319 (1998).
- [42] D. a. Fedosov, I. V. Pivkin, and G. E. Karniadakis, Velocity limit in DPD simulations of wall-bounded flows, *J. Comput. Phys.* **227**, 2540 (2008).
- [43] D. R. Oliver, Influence of particle rotation on radial migration in the poiseuille flow of suspensions, *Nature (London)* **194**, 1269 (1962).
- [44] J. Zhou and I. Papautsky, Fundamentals of inertial focusing in microchannels, *Lab Chip* **13**, 1121 (2013).
- [45] D. Alexeev, L. Amoudruz, S. Litvinov, and P. Koumoutsakos, Mirheo: High-performance mesoscale simulations for microfluidics, *Comput. Phys. Commun.* **254**, 107298 (2020).
- [46] L. Amoudruz, A. Economides, G. Arampatzis, and P. Koumoutsakos, The stress-free state of human erythrocytes: Data-driven inference of a transferable rbc model, *Biophys. J.* **122**, 1517 (2023).
- [47] L. Amoudruz, A. Economides, and P. Koumoutsakos, The volume of healthy red blood cells is optimal for advective oxygen transport in arterioles, *Biophys. J.* **123**, 1289 (2024).
- [48] L. Amoudruz, Simulations and control of artificial microswimmers in blood, Ph.D. thesis, ETH Zurich, 2022.
- [49] C. E. Rasmussen, Gaussian processes in machine learning, in *Advanced Lectures on Machine Learning: ML Summer Schools 2003, Canberra, Australia, February 2-14, 2003, Tübingen, Germany, August 4-16, 2003, Revised Lectures*, edited by O. Bousquet, U. von Luxburg, and G. Rätsch (Springer, Berlin Heidelberg, 2004), pp. 63–71.
- [50] C. Prohm, N. Zöller, and H. Stark, Controlling inertial focussing using rotational motion, *Eur. Phys. J. E* **37**, 36 (2014).
- [51] L. Zeng, S. Balachandar, and P. Fischer, Wall-induced forces on a rigid sphere at finite Reynolds number, *J. Fluid Mech.* **536**, 1 (2005).

- [52] L. Zeng, F. Najjar, S. Balachandar, and P. Fischer, Forces on a finite-sized particle located close to a wall in a linear shear flow, *Phys. Fluids* **21**, 033302 (2009).
- [53] H. Lee and S. Balachandar, Drag and lift forces on a spherical particle moving on a wall in a shear flow at finite Re, *J. Fluid Mech.* **657**, 89 (2010).
- [54] Y.-S. Choi, K.-W. Seo, and S.-J. Lee, Lateral and cross-lateral focusing of spherical particles in a square microchannel, *Lab Chip* **11**, 460 (2011).